Carrier Frequency Offset Compensation for OSDM in Underwater Acoustic Communications: Theory and Experiments Using a Vector MIMO Modem

Zhuoran Qi[†], Rami Rashid[§], Ali Abdi[§], Dario Pompili[†]
Emails: [†]{zhuoran.qi, pompili}@rutgers.edu; [§]{raa62, ali.abdi}@njit.edu
[†]*Department of Electrical and Computer Engineering, Rutgers University, New Brunswick, NJ, USA*
[§]*Department of Electrical and Computer Engineering, New Jersey Institute of Technology, Newark, NJ, USA*

***Abstract*—Underwater acoustic communications suffer from time-varying multipath delay and different Doppler frequency offsets at different paths. To address these issues, a Carrier Frequency Offset Compensated Orthogonal Signal Division Multiplexing (CFO-C-OSDM) is proposed based on the basis expansion model for the time-varying channel. The CFO-C-OSDM method performs CFO compensation and channel estimation jointly, which manages a dynamic Doppler shift range characterized by a nonzero main CFO and residual CFOs caused by multipath propagation effectively. To validate the efficacy of this proposal, several rounds of emulations and experiments were conducted. The results show that the proposed CFO-C-OSDM proves to be more robust against doubly spread channels than existing techniques, such as D-OSDM and OSDM.**

***Index Terms*—Underwater acoustic communications, orthogonal signal division multiplexing, doubly spread channel, carrier frequency offset compensation.**

I. Introduction

Overview: Underwater wireless communications have demonstrated significant potential by offering the advantage of unrestricted flexibility in system development, such as adaptable communication ranges and deployment locations, enabling dynamic and versatile exploration and monitoring capabilities [1], [2]. There are four main technologies to enable underwater communications: Underwater Radio Frequency Communication (URFC), Underwater Magnetic Induction Communication (UMIC), Underwater Optical Wireless Communication (UOWC), and Underwater Acoustic Communication (UAC). URFC operates within a bandwidth of several MHz and achieves data rates up to $100\ \mathrm{Mbps}$ [3], making it suitable for short-range communications in shallow water. However, URFC suffers from high attenuation due to the high conductivity and permittivity of seawater, limiting its coverage range to approximately $10\ \mathrm{m}$ and raising concerns about energy efficiency. The UMIC [4] experiences lower signal attenuation compared to URFC and offers low-latency transmission, but its effectiveness is restricted to a short coverage range of a few meters. UOWC provides a wide bandwidth of hundreds of MHz and supports data rates in the Gbps range over distances of up to $100\ \mathrm{m}$ [5], [6]. However, UOWC faces challenges such as attenuation caused by absorption, scattering, and suspended particle reflection. Solar background noise in shallow waters during daytime operations further impacts its performance. UAC is favored for medium- to long-range communications because of its lower attenuation and supporting distances of several kilometers. However, UAC is restricted by narrow bandwidth, low data rates of a few kbps, slow propagation speed of $1,500\ \mathrm{m/s}$, and significant transmission delays. Moreover, a critical challenge in UAC is the doubly spread effects, which include time-varying multipath effects and Doppler effects. Doppler effects are caused by dynamic and unpredictable movements of water, resulting in significant frequency shifts that degrade communication quality [7]. The doubly spread effect, combined with the other inherent limitations of the UAC, underscores the need for robust strategies to address frequency changes and ensure reliable underwater communication performance.

Related Works: To address the challenges posed by Doppler effects, various physical-layer designs have been developed. Orthogonal Frequency-Division Multiplexing (OFDM) is widely adopted for its robustness against multipath delay and high spectral efficiency, and its effectiveness has been proven in UAC [8]. However, OFDM is sensitive to Carrier Frequency Offset (CFO) and Inter-Carrier Interference (ICI) caused by the Doppler effect, especially in dynamic underwater acoustic environments [9]. In [10] and [11], we estimate and compensate for the CFO in OFDM utilizing null subcarriers and assuming that all multipaths share a similar Doppler scaling factor. The optimal scaling factor was determined by minimizing the energy received in the null subcarriers [12]. In contrast, the authors in [13] addressed scenarios where different paths exhibit distinct Doppler scaling factors. Their two-step approach involved (i) compensating for mean Doppler shifts by minimizing the received energy at null subcarriers, based on the assumption that the energy of these subcarriers should ideally be zero, and (ii) correcting residual CFO through channel estimation and equalization, which assumes that the null subcarrier energy is nonzero. However, these two steps are based on conflicting assumptions about the null subcarrier energy, which introduces inconsistency in the compensation process. And inaccuracy in (i) leads to more errors in (ii) subsequently. In addition, OFDM's high Peak-to-Average Power Ratio (PAPR) remains a drawback, leading to nonlinear distortion in power amplifiers. As an alternative technology of OFDM, Orthogonal Signal-Division Multiplex-

ing (OSDM) was introduced, leveraging the orthogonality of the Inverse Discrete Fourier Transform (IDFT) matrix [14]. OFDM can be considered a special case of OSDM. Compared to OFDM, OSDM offers improved robustness against time-varying channels while maintaining a lower PAPR. Based on this, the authors in [15] proposed a Doppler-resilient OSDM (D-OSDM), which mitigates doubly spread effects by modeling channels using a Basis Expansion Model (BEM). However, D-OSDM requires the Doppler shift to remain constrained within a limited range near zero, limiting its effectiveness in highly dynamic environments. To address this limitation, we propose a novel CFO-Compensated OSDM (C-CFO-OSDM) method, which removes the need to constrain the Doppler shift to near-zero values, significantly enhancing its applicability in more dynamic scenarios.

Our Contributions: In this work, we propose and validate the CFO-C-OSDM modulation method, which jointly compensates for the CFO and performs channel estimation to enhance the performance of UAC systems in doubly spread channels. A comprehensive derivation of the CFO-C-OSDM modulator and demodulator equations is provided, using the Kronecker product of the IDFT matrix. The performance of CFO-C-OSDM is evaluated through real-channel emulations and pool experiments. The emulation channels were collected at Barnegat Bay, NJ. The custom-designed transceiver structure for the CFO-C-OSDM experiments is detailed with an accompanying block diagram. Bit Error Rate (BER) performance is analyzed under various CFO settings and motion scenarios. The results of both emulations and experiments confirm that the proposed CFO-C-OSDM method offers enhanced robustness against doubly spread effects in UAC channels.

Paper Organization: Section II introduces the doubly spread channel model. Section III describes our CFO-C-OSDM. Emulation and experiment setups as well as the results are presented in Section IV. Section V concludes the paper.

II. Doubly Spread Channel Model

Let T_s denote the period of the symbol. Assume that the subcarrier spacing is $1/T_s$. The transmit signal in the baseband is expressed by,

$$x(t) = \sum_n s(n;t) e^{2\pi\sqrt{-1}\frac{n}{T_s}t}, \tag{1}$$

where $s(n;t)$ is the transmit signal on the n-th subcarrier. There are N subcarriers in total.

With carrier frequency f_c, the transmit signal in the passband is expressed by,

$$x(t) = \sum_n s(n;t) e^{2\pi\sqrt{-1}\frac{n}{T_s}t} e^{2\pi\sqrt{-1}f_c t}. \tag{2}$$

The time-varying UAC channel can be expressed by,

$$h(\tau;t) = \sum_l h(l;t)\delta(\tau-\tau_l), \tag{3}$$

where $h(l;t)$ is the channel response at l-th path.

Ignoring noise, the received passband signal without Doppler effects is,

$$\tilde{y}(t) = \sum_l h(l;t) \sum_n s(n;t) e^{2\pi\sqrt{-1}\frac{n}{T_s}(t-\tau_l)} e^{2\pi\sqrt{-1}f_c(t-\tau_l)}. \tag{4}$$

Consider that the Doppler scales $b_l = \Delta f_l / f_c$ are different on different paths, Δf_l is the Doppler frequency shift. The received signal with Doppler effects can be expressed by [13],

$$\begin{aligned}\hat{y}(t) = &\sum_l h(l;t) \sum_n s(n;t) e^{2\pi\sqrt{-1}\frac{n}{T_s}((1+b_l)t-\tau_l)} \\ &\times e^{2\pi\sqrt{-1}f_c((1+b_l)t-\tau_l)}.\end{aligned} \tag{5}$$

After down-conversion with f_c, the received signal in the baseband is,

$$\begin{aligned} y(t) =& \sum_l h(l;t) \sum_n s(n;t) e^{2\pi\sqrt{-1}\frac{n}{T_s}((1+b_l)t-\tau_l)} \\ &\times e^{2\pi\sqrt{-1}f_c(b_l t-\tau_l)} \\ =& \sum_l \hat{h}(l;t) \sum_n s(n;t) e^{2\pi\sqrt{-1}\frac{n}{T_s}(t-\tau_l)} e^{2\pi\sqrt{-1}\frac{n}{T_s}b_l t}, \\ \hat{h}(l;t) =& h(l;t) e^{2\pi\sqrt{-1}f_c(b_l t-\tau_l)} = h(l;t) e^{2\pi\sqrt{-1}(\Delta f_l t - f_c\tau_l)}, \end{aligned} \tag{6}$$

where we can observe that the Doppler frequency shifts are different for different subcarriers at different paths.

Assume M is the length of the message block, $\bar{D}$ is the main CFO, D is the maximum residual CFO, $\bar{D}-D \le MN(b_l + \Delta f_l T_s) \le \bar{D}+D$ for $l = 0,1,...,L$, $L \le M$, $2D+1 < N$, $b_l = 0$ and $\hat{h}(l;t) = 0$ for $l > L$. Consider utilizing Cyclic Prefix (CP) to defend against Inter-Symbol Interference (ISI) caused by multipath delay, the equivalent discrete-time system for an MN-point data block can be expressed by,

$$\mathbf{y} = \mathbf{x}\mathbf{H}_T \mathbf{\Lambda}_{\bar{D}}, \tag{7}$$

where $\mathbf{\Lambda}_{\bar{D}} = \mathrm{diag}([0 \quad W_{MN}^{\bar{D}} \quad W_{MN}^{2\bar{D}} \quad \cdots \quad W_{MN}^{(MN-1)\bar{D}}])$, $W_{MN}^{i\bar{D}} = e^{2\pi\sqrt{-1}\frac{i\bar{D}}{MN}}$, $i = 0,1,...,MN-1$, $\mathrm{diag}(\cdot)$ denotes diagonal matrix. $\mathbf{H}_T$ is a circulant matrix defined by $\mathbf{H}$, which collecting all the time variation of channel taps in (6),

$$\begin{aligned} &\mathbf{H} = [\boldsymbol{h}_{T,0},\ \boldsymbol{h}_{T,1},\ \cdots,\ \boldsymbol{h}_{T,MN-1}], \\ &\mathbf{H}_T[i,j] = \mathbf{H}[j, \mathrm{mod}(j-i, MN)], \\ &i = 0,1,...,MN-1, \quad j = 0,1,...,MN-1, \end{aligned} \tag{8}$$

where $\boldsymbol{h}_{T,l}$ is the l-th channel tap of size $MN \times 1$, $\boldsymbol{h}_{T,l} = \mathbf{O}_{MN\times 1}$ for $l \ge L$.

Based on BEM channel model [16], the time-domain channel tap $\boldsymbol{h}_{T,l}$ can be expressed by,

$$\boldsymbol{h}_{T,l}[i] = \sum_{d=-D}^{D} \boldsymbol{\lambda}_d[i] \boldsymbol{h}_{F,l}[d], \tag{9}$$

where $\boldsymbol{\lambda}_d[i] = W_{MN}^{id} = e^{2\pi\sqrt{-1}\frac{id}{MN}}$, $\boldsymbol{h}_{F,l}$ is the channel tap in frequency domain. $\boldsymbol{h}_{F,l}[d] = 0$ for $|d| > D$.

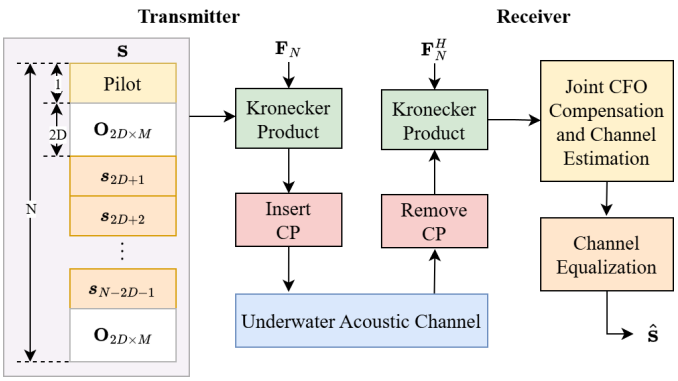

Fig. 1: Block diagram of CFO-C-OSDM at transmitter and receiver: $\mathbf{F}_N$ is the IDFT matrix and $\mathbf{F}_N^H$ is the transpose conjugate of $\mathbf{F}_N$.

If we substitute (9) into (8), we obtain,

$$\mathbf{H}_T = \sum_{d=-D}^{D} \mathbf{H}_{F,d}\mathbf{\Lambda}_d, \tag{10a}$$

$$\mathbf{H}_{F,d} = \begin{bmatrix} h_{F,0,d} & h_{F,1,d} & \cdots & h_{F,MN-1,d} \\ h_{F,MN-1,d} & h_{F,0,d} & \cdots & h_{F,MN-2,d} \\ \vdots & \vdots & \ddots & \vdots \\ h_{F,1,d} & h_{F,2,d} & \cdots & h_{F,0,d} \end{bmatrix}, \tag{10b}$$

where $\mathbf{\Lambda}_d = \mathrm{diag}(\boldsymbol{\lambda}_d)$, $h_{F,l,d} = \boldsymbol{h}_{F,l}[d]$. The received sequence can be expressed by,

$$\mathbf{y} = \mathbf{x}\left(\sum_{d=-D}^{D} \mathbf{H}_{F,d}\mathbf{\Lambda}_d\right)\mathbf{\Lambda}_{\bar{D}}. \tag{11}$$

III. CFO Compensation in OSDM

In this section, we present the design of the proposed CFO-C-OSDM modulator and demodulator. As illustrated in Fig. 1, the modulator inserts parallel sequences into both the time and frequency domains using the Kronecker product with the IDFT matrix. Pilot sequences and Zero Padding (ZP) are employed to facilitate the estimation of the doubly spread channel response. The CP is appended to counter the effects of ISI. In the demodulator, joint CFO compensation and channel estimation are performed using the received pilot sequences. After channel equalization, the demodulated symbols are extracted. The detailed processes of CFO-C-OSDM modulation and demodulation are described in the following.

Modulation: Let $\mathbf{s}$ represent the transmitted sequence,

$$\mathbf{s} = [\boldsymbol{s}_0 \quad \boldsymbol{s}_1 \quad \ldots \quad \boldsymbol{s}_{N-1}], \tag{12}$$

where $\boldsymbol{s}_n$ is the transmit signal at the n-th subcarrier, $n = 0, 1, ..., N-1$, $\boldsymbol{s}_n = [s_{n,0} \quad s_{n,1} \quad \ldots \quad s_{n,M-1}]$.

As shown in Fig. 1, let $\boldsymbol{s}_0$ be the pilot sequence for channel estimation, $[\boldsymbol{s}_1, \cdots, \boldsymbol{s}_{2D}]$ and $[\boldsymbol{s}_{N-2D}, \cdots, \boldsymbol{s}_{N-1}]$ be ZP sequences, and $[\boldsymbol{s}_{2D+1}, \cdots, \boldsymbol{s}_{N-2D-1}]$ be message sequences. Based on OSDM modulation, the transmitted signal is created by the Kronecker product with IDFT matrix. Define $\mathbf{F}_N$ as the IDFT matrix with a size of $N \times N$, $\boldsymbol{f}_n$ is the n-th row of $\mathbf{F}_N$.

$$\mathbf{F}_N = \begin{bmatrix} \boldsymbol{f}_0 \\ \boldsymbol{f}_1 \\ \vdots \\ \boldsymbol{f}_{N-1} \end{bmatrix} = \frac{1}{\sqrt{N}} \begin{bmatrix} W_N^0 & W_N^0 & \cdots & W_N^0 \\ W_N^0 & W_N^1 & \cdots & W_N^{N-1} \\ \vdots & \vdots & \ddots & \vdots \\ W_N^0 & W_N^{N-1} & \cdots & W_N^{(N-1)^2} \end{bmatrix}$$
$$W_N^n = e^{2\pi\sqrt{-1}\frac{n}{N}}, \ n = 0, 1, ..., N-1. \tag{13}$$

The transmitted sequence $\mathbf{x}$ is obtained by,

$$\mathbf{x} = \sum_{n=0}^{N-1} \boldsymbol{f}_n \otimes \boldsymbol{s}_n = \mathbf{s}(\mathbf{F}_N \otimes \mathbf{I}_M), \tag{14}$$

where "$\otimes$" denotes the Kronecker product, $\mathbf{I}_M$ is the identity matrix of size $M \times M$. This transformation organizes the pilot and data symbols in the time and frequency domains with appropriate guard bands, minimizing ICI between them.

Demodulation: When $\bar{D} = 0$, substitute (14) to (11) and let $\mathbf{r}$ be the transformed received sequence,

$$\begin{aligned} \mathbf{r} &= \mathbf{y}(\mathbf{F}_N^H \otimes \mathbf{I}_M) \\ &= \mathbf{s}\sum_{d=-D}^{D} (\mathbf{F}_N \otimes \mathbf{I}_M)\mathbf{H}_{F,d}\mathbf{\Lambda}_d(\mathbf{F}_N^H \otimes \mathbf{I}_M) = \mathbf{s}\mathbb{H}, \end{aligned} \tag{15}$$

where

$$\mathbb{H} = \sum_{d=-D}^{D} \mathbb{H}_d \mathbf{Z}_{MN}^{Md}, \tag{16a}$$

$$\mathbb{H}_d = \mathrm{Diag}\left(\mathbb{H}_{d,0}, \mathbb{H}_{d,1}, \cdots, \mathbb{H}_{d,N-1}\right), \tag{16b}$$

$$\mathbb{H}_{d,n} = \begin{bmatrix} h_{F,0,d} & h_{F,1,d} & \cdots h_{F,M-1,d} \\ W_N^{-n}h_{F,M-1,d} & h_{F,0,d} & \cdots h_{F,M-2,d} \\ \vdots & \vdots & \ddots \quad \vdots \\ W_N^{-n}h_{F,1,d} & W_N^{-n}h_{F,2,d}\cdots & h_{F,0,d} \end{bmatrix} \tilde{\mathbf{\Lambda}}_d,$$
$$\tilde{\mathbf{\Lambda}}_d = \mathrm{diag}([0 \quad W_{MN}^d \quad W_{MN}^{2d} \quad \cdots \quad W_{MN}^{(M-1)d}]). \tag{16c}$$

Here, $\mathrm{Diag}(\cdot)$ denotes the block diagram matrix and $\mathbf{Z}_{MN}$ is the left cyclic shift matrix of size $MN \times MN$, i.e.,

$$\mathbf{Z}_{MN} = \begin{bmatrix} 0 & 1 & 0 & \cdots & 0 \\ 0 & 0 & 1 & \cdots & 0 \\ \vdots & \vdots & \vdots & \ddots & 0 \\ 0 & 0 & 0 & \cdots & 1 \\ 1 & 0 & 0 & \cdots & 0 \end{bmatrix}. \tag{17}$$

Using (12) and (15), we obtain,

$$\begin{aligned} \mathbf{r} &= [\boldsymbol{r}_0, \ \boldsymbol{r}_1, \ \cdots, \ \boldsymbol{r}_{N-1}] \\ &= [\boldsymbol{r}_{0\to D}, \ \boldsymbol{r}_{D+1}, \ \cdots, \ \boldsymbol{r}_{N-D-1}, \ \boldsymbol{r}_{-D\to -1}] \\ &= \mathbf{s}\sum_{d=-D}^{D} \mathrm{Diag}\left(\mathbb{H}_{d,0}, \mathbb{H}_{d,1}, \cdots, \mathbb{H}_{d,N-1}\right)\mathbf{Z}_{MN}^{Md}. \end{aligned} \tag{18}$$

TABLE I: Parameters setting for emulations and experiments.

Parameter	Emulation	Experiment
Distance	10 m	15 m
Depth	0.4 m	0.5 m
Center frequency f_c	100 kHz	20 kHz
Bandwidth B_w	100 kHz	4 kHz
Sampling frequency	400 kHz	102.4 kHz
RRC roll-off factor β	0.25	0.2
Message block length M	64	256
IDFT size N	8	8
Constellation mapping	QPSK	QPSK

Based on (18), $[\boldsymbol{r}_{-D\to -1},\ \boldsymbol{r}_{0\to D}]$ represents the doubly-spread pilot sequence, which can be expressed as,

$$[\boldsymbol{r}_{-D\to -1},\ \boldsymbol{r}_{0\to D}] = \boldsymbol{s}_0\,[\mathbb{H}_{-D,0},\ \mathbb{H}_{-D+1,0},\ \cdots,\ \mathbb{H}_{D,0}]\,. \tag{19}$$

Joint CFO Compensation and Channel Estimation: Let $\boldsymbol{s}_0$ be a Zero Correlation Zone (ZCZ) sequence of length M, $\mathbb{S}_0$ be the circulant matrix of $\boldsymbol{s}_0$, so we have,

$$\boldsymbol{s}_0[m] = e^{\pi\sqrt{-1}\frac{m^2}{M}},\ m = 0, 1, ..., M-1, \tag{20a}$$

$$\mathbb{S}_0 = \begin{bmatrix} \boldsymbol{s}_0[0] & \boldsymbol{s}_0[1] & \cdots & \boldsymbol{s}_0[M-1] \\ \boldsymbol{s}_0[M-1] & \boldsymbol{s}_0[0] & \cdots & \boldsymbol{s}_0[M-2] \\ \vdots & \vdots & \ddots & \vdots \\ \boldsymbol{s}_0[1] & \boldsymbol{s}_0[2] & \cdots & \boldsymbol{s}_0[0] \end{bmatrix}, \tag{20b}$$

$$\frac{1}{M}\boldsymbol{s}_0\mathbb{S}_0^H = [1,\ 0,\ 0,\ \cdots,\ 0] = \mathbb{I}_{1\times M}. \tag{20c}$$

When $\bar{D} \neq 0$ and considering additive noise $\boldsymbol{\sigma}$, we have,

$$\mathbf{y} = \mathbf{s}\sum_{d=-D}^{D}(\mathbf{F}_N \otimes \mathbf{I}_M)\mathbf{H}_{F,d}\boldsymbol{\Lambda}_d\boldsymbol{\Lambda}_{\bar{D}} + \boldsymbol{\sigma}. \tag{21}$$

Since most of the UAC channels are closed to Rician fading model [17], which has one dominant signal path, $\bar{D}$ can be estimated based on the following optimization problem,

$$\max_{\bar{D}}\ R_h(\bar{D}) = \sum_{d=-D}^{D}||\boldsymbol{h}_d^{\{\mathrm{dom}\}}||^2 / \sum_{d=-D}^{D}||\boldsymbol{h}_d||^2 \tag{22a}$$

$$\text{s.t.}\ \ \tilde{\boldsymbol{r}_d} = \mathbf{y}\boldsymbol{\Lambda}_{\bar{D}}^H(\boldsymbol{f}_d^H \otimes \mathbf{I}_M), \tag{22b}$$

$$\boldsymbol{h}_d = \frac{1}{M}\boldsymbol{r}_d\mathbb{S}_0^H,\quad d = -D, -D+1, ..., D, \tag{22c}$$

$$\mathbb{H}_{d,0} = \mathbf{F}_M^H \mathrm{diag}(\boldsymbol{h}_d\mathbf{F}_M)\mathbf{F}_M, \tag{22d}$$

where $\boldsymbol{h}_d^{\{\mathrm{dom}\}}$ represents the dominant path in $\boldsymbol{h}_d$, and $\boldsymbol{f}_d = \boldsymbol{f}_{\mathrm{mod}(d,N)}$. Therefore, $\mathbb{H}_{d,0}$ can be estimated based on (22d), and $\mathbb{H}_{d,n}$ is consequently obtained based on (16). By referring to (15) and considering the noise variance of σ_N^2, the transmitted sequence can be demodulated by the Minimum Mean Square Error (MMSE) equalizer, i.e.,

$$\hat{\mathbf{s}} = \mathbf{y}\boldsymbol{\Lambda}_{\bar{D}}^H(\mathbf{F}_N^H \otimes \mathbf{I}_M)\mathbb{H}^H(\mathbb{H}\mathbb{H}^H + \sigma_N^2\mathbf{I}_{MN})^{-1}. \tag{23}$$

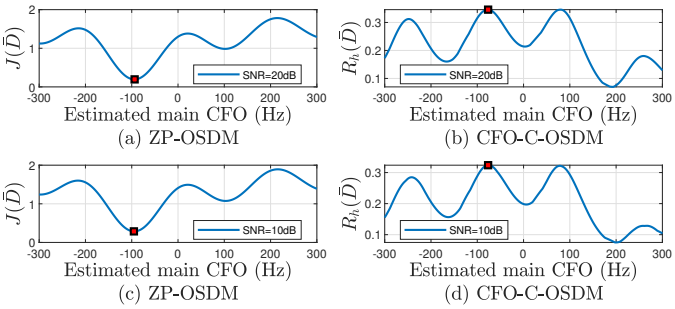

Fig. 2: Optimization process for (a) ZP-OSDM, SNR = 20 dB; (b) CFO-C-OSDM, SNR = 20 dB; (c) ZP-OSDM, SNR = 10 dB; (d) CFO-C-OSDM, SNR = 10 dB;. There is one main CFO at -78 Hz and one residual CFO at 78 Hz, Signal-to-Noise Ratio (SNR) is 20 dB.

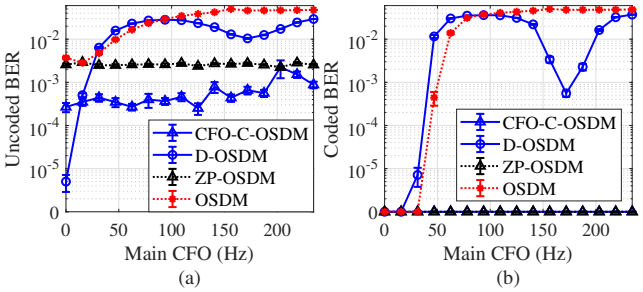

Fig. 3: When SNR = 20 dB, bandwidth B_w = 100 kHz, there is one main CFO and one residual CFO. The Bit Error Rate (BER) performances: (a) Without channel coding. (b) Turbo coding with a code rate of $1/3$.

IV. Performance Evaluation

To validate our proposed CFO-C-OSDM, we performed several rounds of emulations and swimming pool experiments. The CFO-C-OSDM performances of BER are evaluated in comparison with D-OSDM, OSDM with ZP-sequence-based CFO compensation (ZP-OSDM), and OSDM without any CFO compensation. These evaluations are carried out in various settings of CFOs. The parameter setting is detailed in Table I.

Real Acoustic Channel-based Emulations: The UAC doubly spread channels are emulated by feeding real channel taps to the Rician fading channel model. The channel taps are from ACommSet [18] collected from at-sea experiments in Barnegat Bay, New Jersey. The results are provided with 95% confidence intervals to ensure statistical relevance.

Similar to OFDM that utilizes null subcarriers to reduce Doppler shifts [10], the CFO compensation in ZP-OSDM aims to minimize the energy of received ZP sequences, which can be expressed by,

$$\min_{\bar{D}}\ J(\bar{D}) = \sum_{d\in S_{zp}}||\mathbf{y}\boldsymbol{\Lambda}_{\bar{D}}^H(\boldsymbol{f}_d^H \otimes \mathbf{I}_M)||^2, \tag{24}$$

where S_{zp} is the set of ZP sequences. When there is only one main CFO and no residual CFOs, ZP-OSDM works effectively. However, when there are residual CFOs, ZP-OSDM might

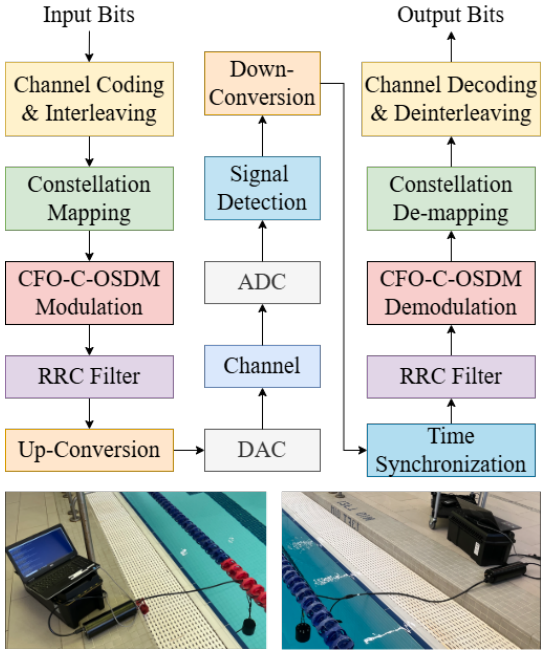

Fig. 4: Experiment transceiver structure. RRC denotes the root-raised-cosine filter. DAC is the digital-to-analog converter, and ADC is the analogy-to-digital converter. Each transmitter/receiver is connected to a laptop.

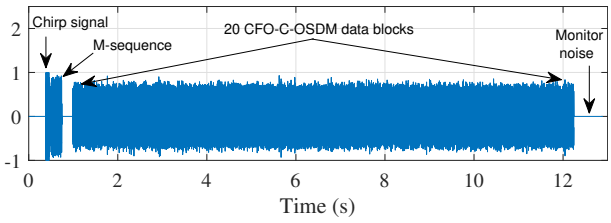

Fig. 5: The transmitted CFO-C-OSDM waveform. A Chirp signal is utilized for signal detection, and M-sequence is utilized for time synchronization.

compensate for CFO inaccurately. In Fig. 2, the channel has one main CFO at -78 Hz and one residual CFO at 78 Hz, SNR$=$ 20 dB. We can observe that ZP-OSDM estimates the main CFO as -93.8 Hz when SNR $=$ 20 dB and -95.3 Hz when SNR $=$ 10 dB. CFO-C-OSDM estimates the main CFO as -76.6 Hz when SNR $=$ 20 dB and 10 dB, which is more accurate than ZP-OSDM. We can observe that there are two peaks in the CFO-C-OSDM optimization process, which correspond to the two CFO components, respectively. Fig. 3(a) depicts the BER without channel coding with varying CFO settings. We can observe that when the CFO is nonzero, the CFO-C-OSDM performs better than ZP-OSDM. Since D-OSDM and OSDM do not do CFO compensation, the BER increases with nonzero CFOs. Note that the residual CFO is nonzero when the main CFO is zero. In Fig. 3(b), we applied turbo channel coding [19] at the rate of $1/3$. We can observe that both CFO-C-OSDM and ZP-OSDM reach zero BER.

Pool Experiments: The custom-designed transceiver structure and transmitted waveform used in our experiments are illustrated in Figs. 4 and 5. In the transmitter, 1/3 turbo channel coding and interleaving are applied to the input bits to improve error correction capabilities. Quadrature Phase Shift Keying (QPSK) is used for constellation mapping to increase the transmission rate. The CFO-C-OSDM modulation process includes the insertion of the pilot and ZP sequences for channel estimation (Fig. 1). To mitigate ISI, Root-Raised-Cosine (RRC) filters with a roll-off factor of $\beta = 0.2$ are employed. The symbol rate is defined as $R_s = B_w/(1+\beta)$, where B_w represents the bandwidth. On the receiver side, signal detection relies on identifying the chirp signal in Fig. 5.

Following down-conversion, time synchronization is achieved by calculating the autocorrelation of the M-sequence [20]. CFO-C-OSDM demodulation involves channel estimation and equalization, followed by constellation de-mapping. The resulting bits are processed through channel decoding (turbo decoding) and de-interleaving to produce the final output. We used a 2×2 vector Multiple-Input Multiple-Output (MIMO) modem [11], whose transmitter is a ring vector transducer that can simultaneously transmit two signals over the x and y vector components of the underwater acoustic field; and its receiver is a transducer, identical to the one used for transmission, that simultaneously measures the components of the underwater acoustic vector x and y. During the experiments, three motion scenarios were tested: (i) Almost no motion at both sides, with only some motion originating from the pool/swimmers; (ii) The transmitter moved at moderate speed forward and backward toward the receiver; (iii) The transmitter moved at a faster speed in random directions. Each scenario was tested in 10 rounds, with 20 CFO-C-OSDM data blocks in each round.

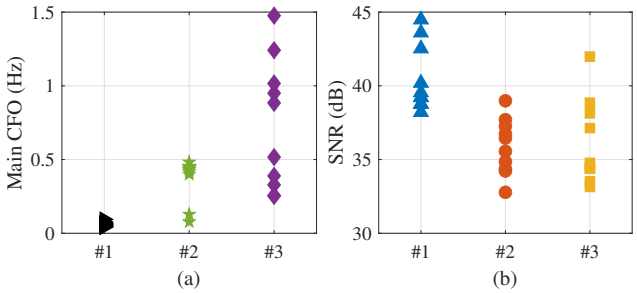

Fig. 6: Motion scenarios: #1. Almost no motion, #2. Forward and backward motion at a moderate speed, and #3. Random motion at a faster speed. Each scenario was repeated for 10 rounds. (a) Estimated CFOs. (b) SNR at receiver.

Fig. 6(a) illustrates the estimated main CFO across three motion scenarios. The CFO is higher during forward and backward motion compared to almost no motion and with a broader spread observed in the case of random motion. Fig. 6(b) shows the received SNR, which decreases as the rapidity of motion increases. Fig. 7 shows the BER performance of various demodulation methods under the three motion scenarios. For almost no motion and without channel

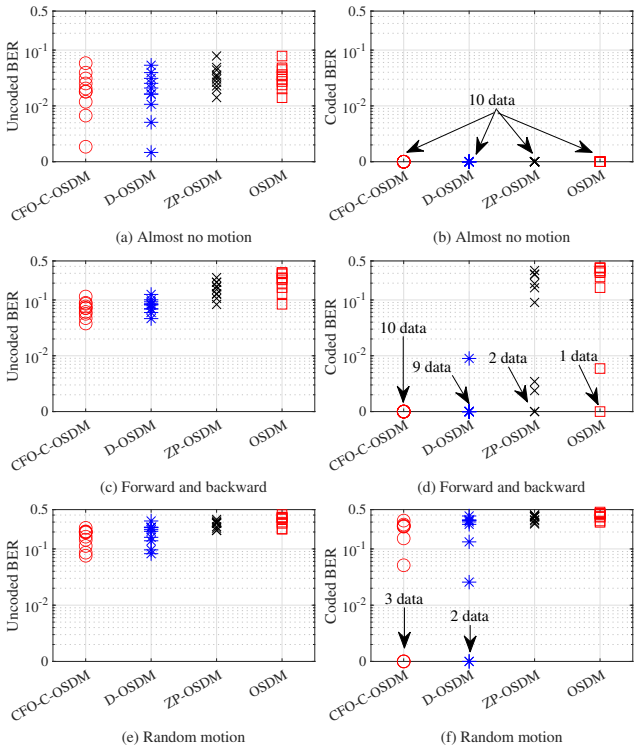

Fig. 7: Bit Error Rate (BER) in the three motion scenarios using different demodulation methods: (a,c,e) without channel coding; (b,d,f) with $1/3$ turbo channel coding.

coding, CFO-C-OSDM performs comparably to D-OSDM and outperforms ZP-OSDM and OSDM. After turbo decoding, all four methods achieve zero BER. In the forward and backward motion scenarios, ZP-OSDM and OSDM exhibit significantly higher BERs. CFO-C-OSDM achieves zero BER after turbo decoding in all 10 rounds, while D-OSDM achieves zero BER in 9 rounds and a nonzero BER in 1 round, indicating that CFO-C-OSDM outperforms D-OSDM. In the random motion scenario, ZP-OSDM and OSDM fail to demodulate effectively. Although the performance of CFO-C-OSDM and D-OSDM deteriorates significantly, CFO-C-OSDM proves to be more reliable than D-OSDM.

V. Conclusion

We proposed a novel Carrier Frequency Offset (CFO) compensation method for underwater OSDM systems, CFO-C-OSDM, to address the challenges posed by doubly spread underwater acoustic channels. By jointly compensating for CFO and estimating the channel, our method enhances the system's robustness against different CFO components caused by multipath delays. Extensive acoustic channel-based emulations and pool experiments in various CFO and motion settings showed that our CFO-C-OSDM outperforms both D-OSDM and ZP-OSDM in mitigating the negative effects of doubly spread acoustic channels on the Bit Error Rate (BER).

Acknowledgment: This work was supported by the NSF NeTS Award No. CNS-1763964.

References

[1] S. Huang, C. Sun, R.-Q. Wang, and D. Pompili, "Multi-behavior multi-agent reinforcement learning for informed search via offline training," *20th International Conference on Distributed Computing in Smart Systems and the Internet of Things (DCOSS-IoT)*, pp. 19–26, 2024.

[2] V. Sadhu, Z. Li, Z. Qi, and D. Pompili, "High-resolution data acquisition and joint source-channel coding in underwater IoT," in *IEEE Internet of Things Journal*, vol. 10, no. 16, 2023, pp. 14 003–14 013.

[3] A. Palmeiro, M. Martín, I. Crowther, and M. Rhodes, "Underwater radio frequency communications," in *OCEANS 2011 IEEE - Spain*, 2011, pp. 1–8.

[4] Y. Li, S. Wang, C. Jin, Y. Zhang, and T. Jiang, "A survey of underwater magnetic induction communications: Fundamental issues, recent advances, and challenges," *IEEE Communications Surveys & Tutorials*, vol. 21, no. 3, pp. 2466–2487, 2019.

[5] H. Kaushal and G. Kaddoum, "Underwater optical wireless communication," in *IEEE Access*, vol. 4, 2016, pp. 1518–1547.

[6] X. Zhao, Z. Qi, and D. Pompili, "Link adaptation in underwater wireless optical communications based on deep learning," *Computer Networks*, vol. 242, pp. 1–11, 2024.

[7] D. Pompili, T. Melodia, and I. F. Akyildiz, "Three-dimensional and two-dimensional deployment analysis for underwater acoustic sensor networks," in *Ad Hoc Networks*, vol. 7, no. 4, 2009, pp. 778 – 790.

[8] Z. Qi, R. Petroccia, and D. Pompili, "RD-ASVTuw: Receiver-driven adaptive scalable video transmission in underwater acoustic networks," *Computer Networks*, vol. 251, p. 110634, 2024.

[9] Y.-T. Hsieh, Z. Qi, and D. Pompili, "ML-based joint Doppler tracking and compensation in underwater acoustic communications," in *Proceedings of the International Conference on Underwater Networks & Systems*, 2022, pp. 1–8.

[10] E. Zhang, R. Rashid, and A. Abdi, "Underwater communication experiments for transmitting multiple data streams using a vector acoustic MIMO system: OFDM and FSK modulations," in *OCEANS 2023 - MTS/IEEE U.S. Gulf Coast*, 2023, pp. 1–5.

[11] E. Zhang, R. Rashid, and A. Abdi, "Particle velocity underwater data communication: Physics, channels, system and experiments," *IEEE Journal of Oceanic Engineering*, vol. 48, no. 4, pp. 1338–1347, 2023.

[12] B. Li, S. Zhou, M. Stojanovic, L. Freitag, and P. Willett, "Multicarrier communication over underwater acoustic channels with nonuniform Doppler shifts," *IEEE Journal of Oceanic Engineering*, vol. 33, no. 2, pp. 198–209, 2008.

[13] Z. Wang, S. Zhou, G. B. Giannakis, C. R. Berger, and J. Huang, "Frequency-domain oversampling for zero-padded OFDM in underwater acoustic communications," *IEEE Journal of Oceanic Engineering*, vol. 37, no. 1, pp. 14–24, 2012.

[14] N. Suehiro, C. Han, and T. Imoto, "Very efficient wireless fyequency usage based on pseudo-coherent addition of multipath signals using Kronecker product with rows of DFT matrix," in *IEEE International Symposium on Information Theory, 2003. Proceedings.*, 2003, pp. 385–385.

[15] T. Ebihara and G. Leus, "Doppler-resilient orthogonal signal-division multiplexing for underwater acoustic communication," *IEEE Journal of Oceanic Engineering*, vol. 41, no. 2, pp. 408–427, 2016.

[16] X. Wang, J. Wang, L. He, and J. Song, "Doubly selective underwater acoustic channel estimation with basis expansion model," in *2017 IEEE International Conference on Communications (ICC)*, 2017, pp. 1–6.

[17] H. Kulhandjian and T. Melodia, "Modeling underwater acoustic channels in short-range shallow water environments," in *Proceedings of the International Conference on Underwater Networks & Systems*, 2014, pp. 1–5.

[18] Z. Qi, K. Anjum, and D. Pompili, "ACommSet: Underwater acoustic communications dataset collection and evaluation in at-sea field experiments," in *Proceedings of the International Conference on Underwater Networks & Systems*, 2024, pp. 1–8.

[19] M. H. Alwan, M. Singh, and H. F. Mahdi, "Performance comparison of turbo codes with LDPC codes and with BCH codes for forward error correcting codes," in *2015 IEEE Student Conference on Research and Development (SCOReD)*, 2015, pp. 556–560.

[20] M. Hamouda, G. Guarin, M. Gardill, B. Läemmle, R. Weigel, D. Kissinger, and T. Ussmueller, "A clock synchronization for M-sequence-based ultra-wideband systems," *IEEE Transactions on Microwave Theory and Techniques*, vol. 62, no. 12, pp. 3549–3561, 2014.